


ARTICLE

DOI: 10.1038/s42005-018-0063-y

OPEN

Anomalous Nernst effect and three-dimensional temperature gradients in magnetic tunnel junctions

Ulrike Martens¹, Torsten Huebner², Henning Ulrichs³, Oliver Reimer², Timo Kuschel², Ronnie R. Tamming⁴, Chia-Lin Chang⁴, Raanan I. Tobey⁴, Andy Thomas⁵, Markus Münzenberg ¹ & Jakob Walowski¹

Localized laser heating creates temperature gradients in all directions leading to three-dimensional electron flux in metallic materials. Temperature gradients in combination with material magnetization generate thermomagnetic voltages. The interplay between these temperature gradients and the magnetization along with their control enable to manipulate the generated voltages in magnetic nanodevices. We present a highly sensitive method to identify the anomalous Nernst effect generated on the nanometer length scale by micrometer-sized temperature gradients in magnetic tunnel junctions with CoFeB electrodes and a MgO tunnel barrier systematically extracted by analyzing the influence of in-plane temperature gradients on the tunnel magneto-Seebeck effect. This method yields an anomalous Nernst effect coefficient of $K_N \approx 1.6 \times 10^{-8} \text{ V T}^{-1} \text{ K}^{-1}$ for CoFeB. Generally, such investigations are motivated by utilizing otherwise wasted heat in magnetic memory devices for read/write operations. The additionally generated anomalous Nernst effect offers a functionality expansion, opening new application fields such as direction-dependent temperature sensing with downscaling potential.

¹Institut für Physik, Universität Greifswald, Felix-Hausdorff-Straße 6, 17489 Greifswald, Germany. ²Center for Spinelectronic Materials and Devices, Physics Department, Bielefeld University, Universitätsstraße 25, 33615 Bielefeld, Germany. ³I. Physikalisches Institut, Georg-August-Universität Göttingen, Friedrich-Hund-Platz 1, 37077 Göttingen, Germany. ⁴Zernike Institute for Advanced Materials, University of Groningen, Nijenborgh 4, 9747 AG Groningen, The Netherlands. ⁵Leibniz Institute for Solid State and Materials Research Dresden (IFW Dresden), Institute for Metallic Materials, Helmholtzstrasse 20, 01069 Dresden, Germany. Correspondence and requests for materials should be addressed to J.W. (email: jakob.walowski@uni-greifswald.de)

Spin-dependent thermally driven transport phenomena have the potential to expand the functionality of today's conventional electronics. A dream of spintronic researchers has been to improve not solely the devices speed, but also enhance power management. This can be accomplished by employing additional energy conversion mechanisms usually available in semiconductor-based integrated circuitry in the form of waste heat. The emerging field of spin caloritronics takes advantage of spin electronic devices in combination with thermal effects. This research field stands at the frontier between thermal transport and spin physics^{1–3}. Magnetic tunnel junctions (MTJs) are one great testbed for spin caloritronic application devices. Originally, they were developed for storage capacity enhancement by the use of the tunnel magnetoresistance effect (TMR)⁴. However, their properties can be directly translated to spin caloritronics when an electric potential as a driving force is replaced by temperature gradients. The thermal method to generate voltage and read out information from MTJs employing temperature gradients utilizes the tunnel magneto-Seebeck effect (TMS). When a temperature gradient is applied across a layer stack of two magnetic electrodes separated by an insulating barrier, the generated voltage V differs, depending on whether the electrodes' magnetizations are aligned parallel (p) or antiparallel (ap). The microscopic origin, together with theoretical predictions of the TMS for multiple CoFe compositions with MgO barriers is given in refs. ^{5,6} and is calculated by:

$$\text{TMS} = \frac{V_{\text{ap}} - V_{\text{p}}}{\min(|V_{\text{ap}}|, |V_{\text{p}}|)}. \quad (1)$$

The TMS effect has been observed and analyzed for various combinations of barrier and electrode materials, showing thermovoltages in the μV range for MgO^{7–13} and MgAl₂O₄^{14–16}, and reaching the mV range for Heusler-based MTJs¹⁷. An overview is given in Kuschel et al.¹⁸. All examined material configurations result in specific TMS ratios. Although MgAl₂O₄ exhibits ratios below 10%, MgO reaches values up to 60%¹⁵ and for electrode combinations CoFeB/MgO/Heusler even ratios of approximately 100% are reported. Meanwhile, the thermal voltage amplitudes approach the order of magnitude that could be used in commercial electronics. Besides this, other effects, e.g., the Onsager reciprocal effect, the tunnel Peltier effect has been realized experimentally¹⁹.

Two preconditions are required to unambiguously achieve enhanced Seebeck voltages in the MTJ's parallel and antiparallel state, V_{p} and V_{ap} ,^{9,11}. One must apply a large temperature gradient across the junction and at the same time, the whole junction area needs to be heated homogeneously. As a consequence, using all-optical laser heating, the spot size needs to be adapted to the junction size and positioned centrally in order to create a well-defined temperature gradient across both electrodes and generate reliable voltages¹¹. Temperature gradients deviating from the out-of-plane direction, e.g., temperature inhomogeneities in the sample plane, lead to further thermoelectric effects that influence the total Seebeck voltages. In this study, we focus on effects generated by these additional in-plane temperature gradients.

There are three thermomagnetic effects that come into question when considering ferromagnetic metal materials whose temperature gradient ∇T and the magnetization M are aligned in the film plane. The first two are the anisotropic magneto thermopower (AMTP) $E_{\text{AMTP}} \propto \nabla T \cdot \cos(\phi_{\nabla T}) M^2 \cdot \cos(2\phi_M)$ and the planar Nernst effect (PNE) $E_{\text{PNE}} \propto \nabla T \cdot \sin(\phi_{\nabla T}) \cdot M^2 \cdot \sin(2\phi_M)$. The angles $\phi_{\nabla T}$ and ϕ_M express the direction of ∇T and M with respect to the direction of voltage measurement. The third is the anomalous Nernst

effect (ANE), $E_{\text{ANE}} \propto \nabla T \times M \propto \nabla T \cdot M \cdot \sin(\phi)$. The angle ϕ denotes the angle between the magnetization M and the temperature gradient ∇T . In the first two configurations, the generated electric fields E_{AMTP} and E_{PNE} are both coplanar with ∇T and M ²⁰, whereas in the last case, the voltage is orthogonal to both, ∇T and M . The former two effects are quadratic in M , which means that magnetization reversal (180° rotation) does not lead to any change of the electric field and thus a reversal of voltage direction. For the ANE, the resulting electric field is perpendicular to the plane defined by ∇T and the M vector, and in contrast to the former two it exhibits a sign change upon magnetization reversal.

In general, ANE experiments are performed with an out-of-plane temperature gradient and the magnetization in the film plane (IM configuration), as well as with in-plane temperature gradients and perpendicular magnetization (PM configuration)^{21,22}. Some publications investigate the aspects of the IM configuration, as published in refs^{23–31} or the PM configuration, as published in^{28,32–34}. In those experiments, usually macroscopic millimeter-sized structures and micrometer wide wires are investigated. The voltage is generated on macroscopic length scales ranging from $>10 \mu\text{m}$ to several millimeters probing predominantly bulk-like properties. In this scope, the ANE measurements in PM CoFeB nanowires with thicknesses below 1 nm play a special role, because those are the smallest dimensions, in which the ANE has been reported so far. There, the temperature gradients are created on length scales up to 500 nm and the generated voltages are detected on length scales in the micrometer range^{35,36}.

Moreover, several publications investigate the ANE enhancement capabilities by utilizing multilayer structures³⁷, by looking at the thickness dependence in different ferromagnetic materials³⁸ or disentangling and quantifying the contributions of other effects, e.g., the thermal Hall effect, to ANE measurements³⁹.

In the present study, we utilize an extended TMS measurement configuration to deliberately create in-plane temperature gradients in MTJ electrodes with in-plane magnetization easy axis and detect the underlying thermomagnetic processes on mesoscopic length scales. This is done by the application of complex three-dimensional temperature gradients to drive spin caloritronic effects in the layered device. We exploit a high flexibility to control both, the magnetization and the temperature gradient direction, and measure the voltages in the lithographically structured MTJ.

Results

Sample geometry and experimental procedure. Figure 1a depicts the sample geometry and the layer sequence to explain the temperature distribution for the discussed heating scenarios and applied magnetic field geometries. In our experimental configuration, the voltage is measured in the out-of-plane direction (defined as z axis), perpendicular to the applied magnetic field $\mu_0 H$ (defined as y axis), whereas the in-plane temperature gradient is rotated in the x - y plane, as defined in Fig. 1b. The access to temperature gradients and the relevant temperature differences is discussed by finite element simulations using COMSOL.

We use pseudo spin valves, because of their most simplistic layer structure and possibility to control the magnetization in both layers of the MTJs. In contrast to exchange biased spin valves, where one magnetic layer is pinned, these devices allow multiple magnetic configurations in the parallel magnetization alignment: with respect to the temperature gradient the magnetization of both ferromagnetic electrodes can be rotated together. We define the thermovoltage measured in the parallel state for direction 1 and 2 as V_{p1} and V_{p2} . The difference

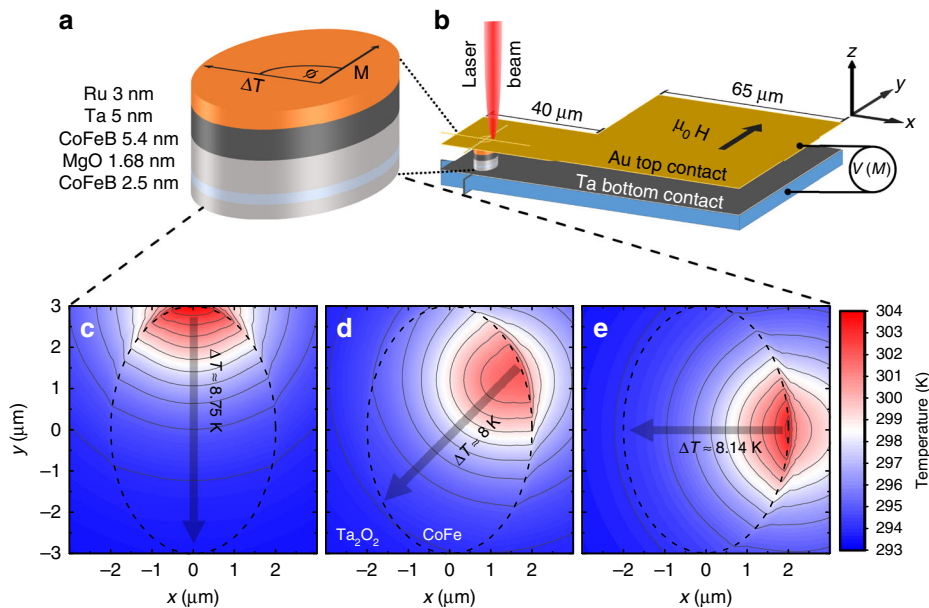


Fig. 1 Sample geometry and in-plane temperature distribution. **a** The MTJ layer stack with the corresponding thicknesses. The magnetization M , with respect to the in-plane temperature gradient ∇T (black arrows) their relation is given by the in-plane varied angle ϕ . **b** MTJ between the Au top and the Ta bottom contacts. The direction of the incoming laser beam, the external magnetic field $\mu_0 H$ and the thermovoltage measurement configuration are indicated within the coordinate axes. **c–e** False color plots showing the in-plane temperature gradients in the top CoFeB electrode for three heating laser spot positions at the junction edges obtained from COMSOL simulations. The MTJ areas are indicated by the dashed lines. Heating at the end of the long (short) axis results in the main temperature gradient in y -direction (x -direction) as shown in **c** (**e**) and indicated by the black arrows. Graph **d** shows the scenario, when the heating laser spot is placed on the edge between both major ellipses axes, resulting in the main temperature gradient at an angle between the two

$\Delta V_{ANE} = V_{p1} - V_{p2}$ is employed in the following to disentangle and characterize thermomagnetic effects that arise from in-plane temperature gradients created in the plane of the electrodes. Additional experimental data identifying the uniaxial magnetic anisotropy (UMA) present in the investigated samples is discussed in a section below.

Temperature distribution. The key feature to analyze spin caloritronic effects in MTJs is the access to temperature distributions on micrometer to nanometer length scales. TMR junctions provide a rich variety of possibilities to create anisotropic temperature profiles on nm to μm length scales using position-dependent laser heating. Extending the scanning technique originally developed for the extraction of the preferably pure TMS signal, as introduced in ref.¹¹, allows a systematic temperature gradient variation. The schematic in Fig. 1b depicts this experimental procedure. In general, a centrally positioned laser spot creates a temperature gradient through the layer stack in z -direction that generates a magnetization-dependent voltage $V(M)$, which can be varied by sweeping an external magnetic field $\mu_0 H$ applied in y -direction. The MTJ layer stack itself is embedded into Au and Ta contact pads and surrounded by insulating Ta_2O_5 in the x - y plane. The Au pads thickness is around three times larger than the optical penetration depth $\lambda_{\text{opt}} \approx 15\text{--}20\text{ nm}$, leaving purely thermal excitation in the CoFeB layers. This sample design allows to create and steadily vary temperature gradients in the x - y plane by moving the laser spot along the surface. The voltage generated at the CoFeB electrodes is measured in z -direction. Due to this configuration, the main voltage contribution generated by in-plane temperature gradients stems from the ANE. Both the AMTP and the PNE can be disregarded, because the voltage is generated in the x - y plane, and only second-order processes with amplitudes that are orders of magnitude smaller can contribute to the out-of-plane signal. For the

investigation of inhomogeneous laser heating, the setup parameters need additional adjustment. The modulated continuous wave laser spot is focused down to $2\ \mu\text{m}$ in diameter and systematically scanned across the sample within an area of $30 \times 30\ \mu\text{m}^2$ in which the elliptically shaped MTJ itself has a dimension of $6\ \mu\text{m}$ by $4\ \mu\text{m}$. Performing such a two-dimensional scan, a local heating point is moved over the entire MTJ area and enables the creation of specifically directed and consistently varied temperature gradients. This allows us to apply complex three-dimensional temperature profiles at will. The situation is discussed in the following example when we place the laser spot at the MTJ's edge.

Figure 1a shows an enlargement of the elliptically shaped MTJ layer stack. The tunnel junction consists of the CoFeB/MgO/CoFeB stack, the Ta layer is necessary to remove boron during crystallization from the CoFeB/MgO interface and lastly the Ru capping is deposited to prevent oxidation during the ex situ annealing process and patterning. The in-plane ∇T together with the in-plane M and the angle ϕ are sketched on top of the stack. Note, that during the measurement, the direction of M remains constant, whereas ∇T is rotated by $\phi = 0^\circ\text{--}360^\circ$. The access to temperature in such small devices is not available experimentally, therefore, three-dimensional finite element simulations using the COMSOL package with the heat transfer module are performed to gain insight into the temperature distribution within the MTJ. The simulations are performed for continuous wave laser heating in equilibrium using the parameters given in the Supplementary Table 1.

Figures 1c–e display the temperature distribution for three different laser spot positions located at the MTJ edges. The false color plots show the equilibrium temperature distribution inside the top CoFeB electrode, which is indicated by the dashed lines. The temperature distribution in the bottom CoFeB shows the same characteristics and is not shown here. However, due to ∇T created in the out-of-plane direction, the overall T is slightly lower. The difference in temperature between top and bottom

electrodes ranges from $\Delta T_{\text{top-bottom}} \approx 50$ mK in the vicinity of the laser spot to <1 mK at the opposite edge and decreases exponentially to a first approximation. However, the temperature distribution simulations reveal that the temperature profiles are more complicated and show strong fluctuations especially at the edges, as discussed in more detail in the Supplementary Note 1 and shown in Supplementary Figures 1–4. As the dimensions in the x-y plane are three orders of magnitude larger, the in-plane temperature differences are larger than those across the layer stack. The temperature gradient directions for each heating scenario are indicated by the gray arrows accompanied by the temperature drop ΔT between both junction edges.

Figure 1c describes the first scenario, when the laser spot is located at the vertex, then a temperature gradient along the major axis with a temperature difference $\Delta T \approx 9$ K is created. Figure 1d shows the second heating scenario when the laser spot is located at the edge of the ellipse at a 45° angle between both principal axes. Consequently, this results in a temperature gradient along the MTJ diagonal with $\Delta T \approx 8$ K. Finally, Fig. 1e illustrates the third scenario, when the laser spot is located at the co-vertex, resulting in a temperature gradient along the minor axis with $\Delta T \approx 8$ K. The slight temperature differences for these external cases result from the asymmetry in the MTJ's geometry. A thorough temperature profile analysis reveals that independent of the ∇T angle the in-plane temperature gradient covers equally sized areas of the MTJ. Therefore, we expect the number of electrons involved in the process triggered by the in-plane temperature gradient to remain angle independent.

The largest, most homogeneous area with a high temperature gradient across the layer stack is created when the laser spot is located with its center at least $1.7 \mu\text{m}$ away from the MTJ's edge. When heating within this area, effects from in-plane temperature gradients cancel each other out and can be excluded. We conclude that by application of the laser spot at the edge of the tunnel junction, large in-plane gradients can be created and rotated by an arbitrary angle in the x-y plane. For a laser spot at the center, the overall x-y gradient is found to vanish, and we have predominantly a temperature gradient in z-direction.

Anomalous Nernst Effect. The pseudo spin valves selected in this study allow for the full directional manipulation of the magnetization in both electrodes, because in contrast to conventional MTJ design, none of the magnetic layers is antiferromagnetically pinned. The condition for their antiparallel magnetization alignment is realized by choosing specially designed electrodes with different anisotropy strength and thus different coercive fields. In the presented investigation both CoFeB layers differ in thicknesses by around 2 nm to fulfill this criterion. This allows two parallel magnetization alignment configurations of opposite direction.

Figure 2a shows an example of a Seebeck voltage vs. external field $\mu_0 H$ sweep, recorded while the laser spot is close to the MTJ edge and a pronounced in-plane temperature gradient is generated, $\phi_{\nabla T} = 90^\circ$. The ranges with parallel and antiparallel magnetization alignment are indicated by the black arrows. For large field amplitudes, both electrodes magnetizations align parallel and a different Seebeck voltage is generated than in the antiparallel alignment. From this measurement curve, the TMS ratio is calculated, which results in a ratio of approximately 50%. This is consistent with the findings reported in ref.¹¹.

The measurement confirms the two possibilities for parallel alignment configuration of opposite direction, V_{p1} for negative $\mu_0 H$ and V_{p2} for positive $\mu_0 H$. Furthermore, the data exhibit a clear shift of V_{p1} with respect to V_{p2} . This voltage shift $\Delta V_{\text{ANE}} = V_{p1} - V_{p2}$ is marked by the shaded blue area. Data recorded with the heating laser spot positioned in the MTJ's center are shown in Supplementary

Figure 5. There, $\Delta V_{\text{ANE}} = 0$, as expected. We argue that ΔV_{ANE} originates from the in-plane temperature gradient, which affects the voltage in the perpendicular direction for parallel magnetization states of opposite sign. At this point, we rule out the PNE and the AMTP for two reasons. First, their quadratic dependence on the magnetization $\sim M^2$ would not result in a difference between V_{p1} and V_{p2} upon magnetization reversal. Second, the voltage is measured perpendicularly to the plane that is spanned by ∇T and M . This perpendicular voltage is zero for PNE and AMTP. Conclusively, we state that ΔV_{ANE} originates from the ANE.

Recently, also the spin Nernst effect (SNE) was verified experimentally at heavy metal/ferromagnet interfaces for ferromagnet insulators (YIG)⁴⁰, and for metallic ferromagnets (CoFeB)^{41,42}. There, an in-plane temperature gradient generates a transverse spin current density in the heavy metal, which influences the generated Seebeck voltage or the Hall resistance of the ferromagnetic layer. However, the Ta/CoFeB interface investigated in ref.⁴¹ shows an SNE that is lower than $0.1 \mu\text{V}$ at an applied temperature difference in the Kelvin range. Because the calculated in-plane temperature gradients in our sample system are two orders of magnitude smaller, we rule out any detectable contribution of the SNE to the ANE extracted from our experiments.

The laser spot is moved over the sample surface and the in-plane temperature gradient is varied, as analyzed in the previous section from the finite element temperature simulations. From each curve, one ΔV_{ANE} value is extracted and plotted in Fig. 2b. In each measurement, the magnetization is reversed together with $\mu_0 H$ along the y axis, as depicted by the black double arrow next to the graph. Figure 2b is divided into two parts.

In the first part, the extracted ΔV_{ANE} values for each heating scenario are illustrated in a three-dimensional surface plot. The spatial position for the ΔV_{ANE} value extracted from Fig. 2a is indicated by the gray dotted lines pointing to Fig. 2b. The voltage difference ΔV_{ANE} shows an increase and a decrease with absolute value maxima of around $0.4 \mu\text{V}$ showing an inversion symmetry regarding the origin of the coordinate system.

In the second part, the same data are projected at the bottom in a false color plot for a better overview. This depiction includes a contour of the MTJ's elliptical area with both principal axes (dashed dark gray crossed lines). Without loss of generality, the angle $\phi_{\nabla T} = 0^\circ$ is defined along the positive y axis and parallel to the positive $\mu_0 H$ and the $\phi_{\nabla T}$ rotation is marked in counter clockwise direction. Both extreme values of ΔV_{ANE} are generated when the laser heating spot is located near the MTJ's edge, where the largest in-plane temperature differences are created (compare COMSOL simulations in Figs. 1c–e) and at $\phi_{\nabla T} = 90^\circ$ and $\phi_{\nabla T} = 270^\circ$. The borderline between the elevation and decrease where $\Delta V_{\text{ANE}} \approx 0$ proceeds parallel to $\mu_0 H$ and is perpendicular to the line connecting the extreme ΔV_{ANE} absolute value locations.

As a main result, the ΔV_{ANE} values extracted from the positions marked by the black ellipse contour are plotted vs. the temperature gradient angle $\phi_{\nabla T}$ with respect to the $\mu_0 H$ direction is shown in Fig. 2c. This two-dimensional plot highlights the ΔV_{ANE} sign change upon in-plane ∇T reversal with respect to the magnetization. This behavior confirms the thermomagnetic origin of the extracted effect. Further analysis of the ΔV_{ANE} signal in Fig. 2c validates the ANE effect generated by in-plane temperature gradients. The extracted data (blue dots) are fitted to the formula given by the ANE cross-product definition, when the temperature gradient is rotated by $\phi_{\nabla T}$:

$$\Delta V_{\text{ANE}} = A \cdot \sin(\phi_{\nabla T} - \phi_0) + V_0. \quad (2)$$

The extracted fit parameters are $A = (0.42 \pm 0.04) \mu\text{V}$, the maximum ΔV_{ANE} amplitude, $\phi_0 = (4 \pm 5)^\circ$, the phase shift, which

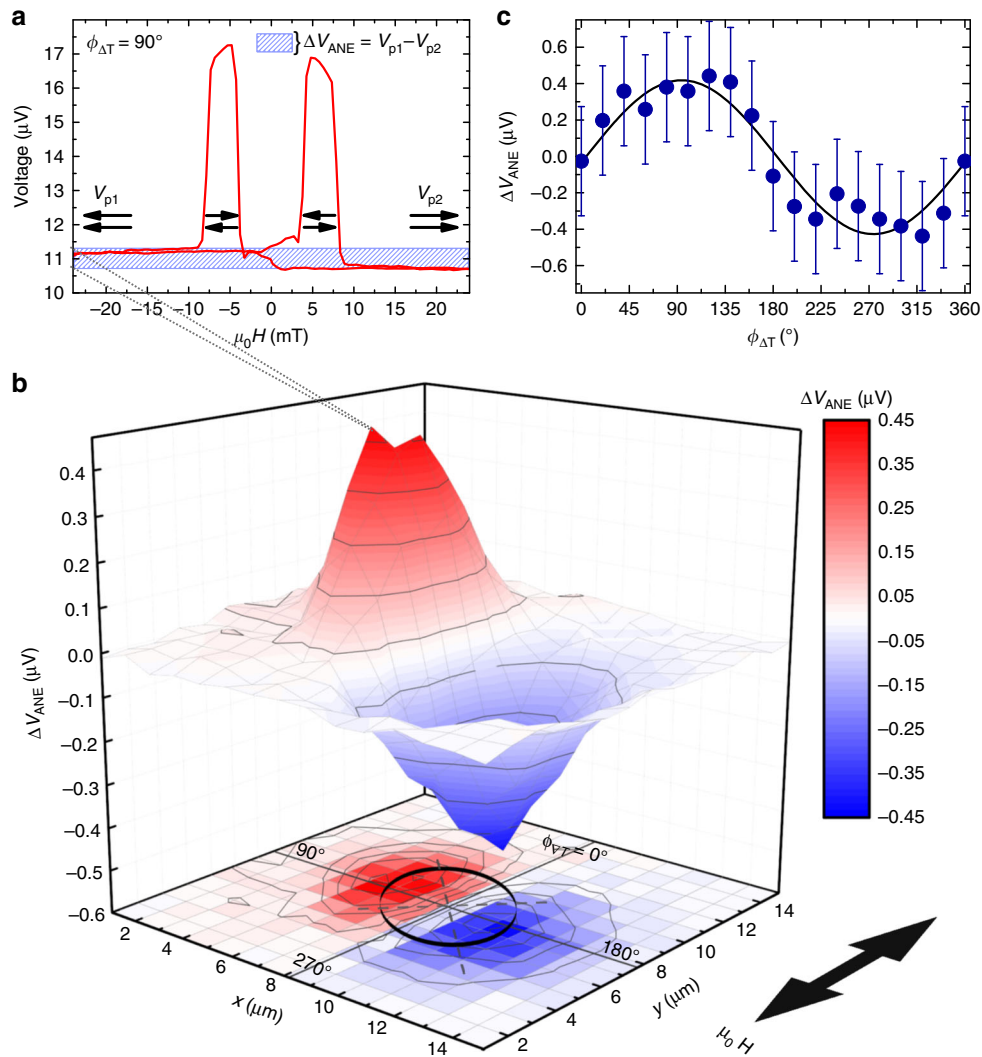


Fig. 2 The ANE effect extracted from TMS measurements. **a** Exemplary TMS measurement curve showing the Seebeck voltage vs. the external field (red line). The ranges with parallel and antiparallel magnetization alignment of both electrodes are indicated by the black arrows. The blue area marks the difference ΔV_{ANE} between the voltage measured in parallel magnetization configuration for both directions V_{p1} and V_{p2} . **b** The extracted ΔV_{ANE} values are plotted vs. the laser position in a three-dimensional surface plot with a false color projection at the bottom. The black ellipse outlines the MTJ area, the gray dashed cross is located along the principal axes. $\phi_{\nabla T}$ indicates the angle between the external field $\mu_0 H$ and the temperature gradient direction. **c** ΔV_{ANE} values extracted along the ellipses contour plotted with error bars against the temperature gradient angle $\phi_{\nabla T}$ together with the fitted sine curve

expresses the angle between the MTJ's magnetization and ∇T when the temperature gradient is aligned parallel to $\mu_0 H$, and $V_0 = (0.00 \pm 0.026) \mu\text{V}$, the offset voltage.

The small value obtained for ϕ_0 indicates an excellent magnetization easy axis alignment with the external field direction. This also reveals that when ∇T and M are aligned parallel or antiparallel, $\Delta V_{\text{ANE}} = 0$. This corresponds to the angles $\phi_{\nabla T} = 0^\circ$ and $\phi_{\nabla T} = 180^\circ$, as indicated in the projection in Fig. 2b. Both maximum amplitudes are located at $\phi_{\nabla T} = 90^\circ$ and $\phi_{\nabla T} = 270^\circ$, when M and ∇T are perpendicular to each other. In conclusion, our findings are consistent with the cross-product definition of the ANE. Besides this, the vanishing offset V_0 confirms the ANEs symmetry with respect to the magnetization direction.

During the course of our measurements, we find that the MTJs possess an in-plane magnetic anisotropy. This is indicated in TMR, as well as in MOKE measurements on CoFeB/MgO films. Additional magnetic anisotropy contributions could also influence the characteristics of the ANE effect.

In order to suppress these contributions to the voltage signal generated by in-plane temperature gradients, we first analyze the magnetic anisotropy for CoFeB thin films deposited on MgO substrates in detail. For this purpose, we prepare a thin CoFeB film sputtered from the same target as those used for the MTJs on an MgO substrate under identical conditions. This film was chosen to be thicker (40 nm) to assure a good signal in all-optical pump-probe experiments. Further, if the crystallization at the MgO/CoFeB interface induces a strong enough uniaxial in-plane anisotropy for a 40 nm thick film, then this will hold even more for thinner CoFeB films. After that, magnetization dynamics experiments, rotating $\mu_0 H$ in the sample plane are performed with an angle resolution of 5° , as depicted in Fig. 3a. Here, the precessional dynamics on the nanosecond time scale are plotted vs. the rotation of $\mu_0 H$ in a false color plot, showing the negative/positive precession amplitude in blue/red. Figure 3b shows the precession frequencies extracted by fast Fourier transform. The frequency amplitudes are false color coded using a different color scheme for a better distinction. In accordance to the analysis

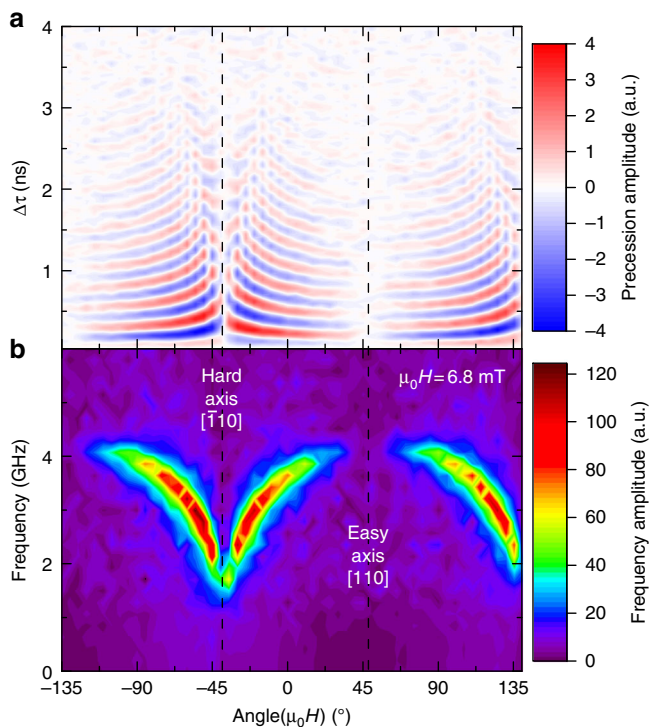


Fig. 3 Magnetic anisotropy determined from magnetization dynamics measurements. **a** Precessional dynamics from all-optical pump-probe experiments recorded for a CoFeB thin film, by rotating the $\mu_0\mathbf{H} = 6.8$ mT in the film plane in steps of 5° . The precession amplitude is coded from negative deflection (blue) to positive deflection (red). **b** The precession frequencies extracted by FFT (different color code for a better distinction). The magnetic hard and easy axes are marked by the dashed black lines. The precession frequency increases towards the magnetic easy axis and declines towards the magnetic hard axis

presented in ref.⁴³, we interpret our data as follows. The plot shows a declining precession frequency near the magnetic hard axis pointing into the $[\bar{1}10]$ direction and frequency increase when $\mu_0\mathbf{H}$ is rotated towards the magnetic easy axis pointing into the $[110]$ direction. The frequency reaches saturation and the amplitude declines in the vicinity of the easy axis, because the applied field amplitude ($\mu_0\mathbf{H} = 6.8$ mT) is sufficient to saturate the sample, but too small to force the magnetization slightly out of the magnetic easy axis. This means, CoFeB grown on MgO exhibits an UMA with the magnetic easy axis along the $[110]$ crystalline direction.

Although the MTJ's elliptic shape is aligned with the vertex along the $[100]$ direction, for a 1.5 vertex/co-vertex ratio and a layer thickness in the nanometer range, the calculated demagnetizing fields due to shape anisotropy are approximately 2 mT, using geometrical considerations given in ref.⁴⁴. Therefore, solely the magneto-crystalline anisotropy remains as a significant factor leaving the magnetic easy axis along the $[110]$ direction. Taking those findings into account, the MTJ is placed with the magnetic easy axis parallel to the applied field $\mu_0\mathbf{H}$ for the ANE measurements.

In addition to this, we also exclude contact resistance or bond wire geometry as an origin for this behavior, because repetition of those measurements with the contact wires attached at different angles to the magnetic field, as well as at various positions and distances from the MTJ all return the same qualitative and quantitative characteristics (not shown here).

Finally, from these findings, the ANE coefficient can be estimated, considering that the CoFeB saturation magnetization is $M_S \approx 1.6$ T and the in-plane temperature difference $\Delta T \approx 8$ K. The maximum ΔV_{ANE} value needs to be divided by two, because the shift in Fig. 2a influences the voltage measured in both parallel magnetization alignment directions. Starting with a homogeneous heating scenario, where the in-plane $\nabla T \approx 0$, also results in $\Delta V_{ANE} = 0$. However, an in-plane $\nabla T \neq 0$ shifts V_{p1} to higher values, whereas it shifts V_{p2} to lower values. Thus, the contribution to the ANE is given by $\frac{1}{2}\Delta V_{ANE}$. This results in an anomalous Nernst coefficient of $K_N = \frac{1}{2}\Delta V_{ANE} M_S^{-1} \Delta T^{-1} \approx 1.6 \times 10^{-8} \text{ V} \cdot \text{T}^{-1} \cdot \text{K}^{-1}$. How does this value compare to previously published results? In 2014, Lee et al. determined the anomalous Nernst coefficients in ferromagnet/non-magnet heterostructures for non-magnet materials with different spin hall angles in the range from $10^{-6} \text{ V T}^{-1} \text{ K}^{-1}$ to $10^{-8} \text{ V T}^{-1} \text{ K}^{-1}$ ²⁷. The value found in our detection scheme through magneto-Seebeck measurements, agrees well with the order of magnitude with these values. However, in their measurement the contributions from the ANE and the spin Seebeck effect are difficult to disentangle. A further look into literature reveals that K_N varies between different materials by several orders of magnitude. For instance, Wells et al. extracted an anomalous Nernst coefficient $K_N = 2.3 \times 10^{-6} \text{ V T}^{-1} \text{ K}^{-1}$ from measurements on perpendicularly (out-of-plane) magnetized amorphous CoFeB nanowires³⁵. For FePt, Mizuguchi et al. and later Sakuraba et al. determined an anomalous Nernst coefficient of $\sim 0.5 \times 10^{-7} \text{ V T}^{-1} \text{ K}^{-1}$ ^{45,46}. A similar value of $\sim 1.3 \times 10^{-7} \text{ V T}^{-1} \text{ K}^{-1}$ ²³ was found by Weiler et al. for Ni. The comparison shows that our experimental method is extremely sensitive. We estimate that even for an anomalous Nernst coefficient as small as $10^{-9} \text{ V T}^{-1} \text{ K}^{-1}$ a detection would be possible.

The two orders of magnitude difference between K_N extracted by Wells et al. and in our experiments have several reasons. The main difference is the amorphous structure of the nanowires, compared with the crystalline MTJs. Electrical and thermal transport properties of amorphous materials differ strongly from crystalline materials; therefore, it is not surprising that the ANE coefficients differ as well. Additionally, spin-orbital coupling is different in all materials compared here. In case of Wells et al., a strong PMA is present, which is stronger than the UMA in the MTJs. Furthermore, there is a difference in temperature determination. They use scanning thermal microscopy to determine the temperature gradients. Due to the sample design and the MTJ size, which is relevant for the experiment, we are compelled to rely on temperature simulations, which can account for further deviations.

Discussion

We investigated how in-plane temperature gradients in single MTJs enhances or decreases the out-of-plane thermovoltage in TMS measurements. The extracted voltage shows a symmetric characteristic that can be clearly attributed to the ANE with respect to the UMA of the sample. This UMA is verified by magnetization dynamics measurements.

Primarily we observe that the ANE affects only the Seebeck voltage in the parallel magnetization alignment and the ANE voltages are two orders of magnitude smaller compared with the TMS voltages. Therefore, the influence on the overall TMS ratio needs to be considered in the analysis if in-plane temperature gradients are present, even if it is small. Nevertheless, the ANE can be clearly identified and extracted from TMS measurements of pseudo spin valve MTJs.

In the case of MTJs with one antiferromagnetically pinned and one switching electrode, the occurrence of ANE due to inhomogeneous heating and the presence of in-plane temperature gradients will lead to a deviation in the magneto-Seebeck voltage from the real value. However, in this configuration it is not possible to disentangle both contributions, as the ANE and the minor TMS loop have the same shape due to the equal magnetic field dependence.

In our experiments, samples with different MgO barrier thicknesses are measured and show qualitatively similar characteristics as is discussed in the Supplementary Note 2 and can be seen in Supplementary Figure 6. From those findings, we conclude that there is no significant influence of the MgO layer thickness on the ANE contribution. However, we are pointing out that an intact MgO barrier is essential for ANE detection, because it is sensed as an influence on the Seebeck voltages measured for the TMS effect. To elucidate the importance, we are showing ANE measurements on an MTJ with broken MgO barrier in Supplementary Figure 7 added to the Supplementary Note 3.

Within this study, we illustrate the first detection of the ANE in MTJs on such short length scales also obtaining a high spatial resolution. These results show very clearly the importance of homogenous laser heating to avoid unintended effects in case of TMS measurements by laser heating. The measurements show a clear dependence of the extracted ANE effect on the angle between the magnetization and the temperature gradient. Together with a proper calibration, and a combination of the investigated effects and technologies enables the construction of a direction-dependent thermometer. This thermometer would not only sense the temperature, but also the direction of change, working as follows. Consider an MTJ in the parallel magnetization alignment for both ferromagnetic layers, subject to a lateral heat flux, which is not necessarily induced by laser heating, and which shall be characterized. The heat flux establishes a temperature gradient in the MTJs plane. As we have discussed above, the lateral temperature gradient generates a voltage in the direction perpendicular to the MTJs plane. This voltage changes from V_{p1} to V_{p2} upon magnetization reversal. As the difference $V_{p1} - V_{p2} = \Delta V_{ANE}$ depends on the angle between magnetization axis and the direction of heat flux, after detecting ΔV_{ANE} for different magnetization directions, the direction of the heat flux can be determined. The suggested device demands a way to set the magnetization in the MTJ at arbitrary in-plane angles. Note, that switching of magnetization could be accomplished by employing spin transfer torque or spin orbit torque switching. In the future, the combination of TMS and ANE measurement will even enable a three-dimensional direction analysis of the effective heat flux by evaluating the relation between the TMS and ANE contribution to the signal. Because of the exponential temperature decay in the sample plane together with the sensitivity of this method, there is room for further device miniaturization beyond the micrometer scale.

Methods

Sample fabrication. The sample stack of the investigated thin films consists of Au 70 nm/Ru 3 nm/Ta 5 nm/CoFeB 5.4 nm/MgO 1.68 nm/CoFeB 2.5 nm/Ta 10 nm/MgO (100) substrate. The CoFeB electrodes are fabricated by magnetron sputtering using 2-inch targets with a composition of $\text{Co}_{0.2}\text{Fe}_{0.8}\text{B}_{0.2}$ (analysis Co:Fe 0.32:0.68). In a separate chamber, the MgO barrier is e-beam evaporated without breaking the vacuum. The Ru capping layer is deposited by e-beam evaporation and prevents the underlying layers from oxidation. Ex situ annealing with applied bias field is performed to crystallize the amorphous CoFeB electrodes and the MgO layer to obtain coherent interfaces and to activate the diffusion of B into the Ta layers^{47–49}. Afterwards, elliptical MTJs are patterned to a size of $6 \mu\text{m} \times 4 \mu\text{m}$ with the long axis parallel to the direction of the magnetic field applied during the annealing by lithography processes. For thermal and electrical isolation, Ta_2O_5 is sputtered in the surroundings of the single MTJs. The Au layer pads on top are necessary to

enable electrical contacting. A detailed description of the sample fabrication can be found in ref.¹¹.

Magneto-Seebeck experiment. For the generation of a temperature gradient across the layer stack, a laser diode (TOPTICA ibeam smart) with a wavelength of 638 nm and a maximum power of 150 mW is used. The laser is focused to a minimum diameter of $\sim 2 \mu\text{m}$ full-width at half-maximum by utilizing a microscope objective (NIKON 20 \times , WD 20.5 mm). The generated thermovoltage is detected with a lock-in amplifier. The laser diode is modulated with a square wave at a frequency of 77 Hz, which is used as modulation frequency for the lock-in amplifier. For magnetization-dependent measurements, the sample is placed in between two pole shoes of an electromagnet. The implemented linear stages with motorized actuators for the horizontal (x-direction) and vertical (y-direction) movement enable an exact positioning of the laser beam on the sample surface together with a high spatial resolution of 0.2 μm . This setup allows the recording of the generated thermovoltage in z-direction depending on the magnetization direction by heating the sample at different positions over a defined area. In this study, the measured area is adapted to the junction size and with respect to the backlash of the actuators a dimension of $30 \mu\text{m} \times 30 \mu\text{m}$ with a resolution of 1 μm is preferred.

Magnetization dynamics. The all-optical pump-probe Faraday configuration uses a 400 nm pump and 800 nm probe beam from a 1 kHz Ti:Sapphire laser system with 120 fs pulse lengths. The pump fluence is $F_{\text{pump}} = 5.7 \text{ mJ cm}^{-2}$. The delay can be varied from 0 to 8 ns. The sample is situated in a constant applied magnetic field, which can be rotated in the sample plane.

Temperature distribution simulations. The temperature distributions were obtained by finite element modeling with the software package COMSOL version 4.2a, including the heat transfer module. Most values for the necessary material parameters (specific heat c , thermal conductivity κ , density ρ) were taken from ref.⁷. For Ta_2O_5 , we assumed $c = 135.6 \text{ J mol}^{-1} \text{ K}^{-1}$, $\kappa = 0.3 \text{ W m}^{-1} \text{ K}^{-1}$, and $\rho = 8270 \text{ kg m}^{-3}$ according to refs.^{50,51}. In contrast to the work presented in ref.⁷, here we implemented a fully three-dimensional model of the junction. The laser heating was taken into account as a volumetric heating source

$H \sim \exp\left(-\frac{z}{\lambda_{\text{opt}}} - \frac{2(x-x_0)^2 + (y-y_0)^2}{w^2}\right)$, where $z = 0$ refers to the surface of the top Au electrode. See further description of the procedure in the Supplementary Note 1.

Data availability

The data that support the plots within this paper and other finding of this study are available from the corresponding author upon reasonable request.

Received: 27 April 2018 Accepted: 3 September 2018

Published online: 15 October 2018

References

- Bauer, G. E. W., Saitoh, E. & van Wees, B. J. Spin caloritronics. *Nat. Mater.* **11**, 391–399 (2012).
- Yu, H., Brechet, S. D. & Ansermet, J.-P. Spin caloritronics, origin and outlook. *Phys. Lett. A* **381**, 825–837 (2017).
- Boona, S. R., Myers, R. C. & Heremans, J. P. Spin caloritronics. *Energy Environ. Sci.* **7**, 885 (2014).
- Miao, G.-X., Münzenberg, M. & Moodera, J. S. Tunneling path toward spintronics. *Rep. Prog. Phys.* **74**, 36501 (2011).
- Czerner, M., Bachmann, M. & Heiliger, C. Spin caloritronics in magnetic tunnel junctions. *Ab initio Stud. Phys. Rev. B* **83**, 132405 (2011).
- Heiliger, C., Franz, C. & Czerner, M. Ab initio studies of the tunneling magneto-Seebeck effect. Influence of magnetic material. *Phys. Rev. B* **87**, 224412 (2013).
- Walter, M. et al. Seebeck effect in magnetic tunnel junctions. *Nat. Mater.* **10**, 742–746 (2011).
- Liebing, N. et al. Tunneling magneto thermopower in magnetic tunnel junction nanopillars. *Phys. Rev. Lett.* **107**, 177201 (2011).
- Boehnke, A. et al. Time-resolved measurement of the tunnel magneto-Seebeck effect in a single magnetic tunnel junction. *Rev. Sci. Instrum.* **84**, 63905 (2013).
- Boehnke, A. et al. On/off switching of bit readout in bias-enhanced tunnel magneto-Seebeck effect. *Sci. Rep.* **5**, 8945 (2015).
- Martens, U. et al. Pumping laser excited spins through MgO barriers. *J. Phys. D: Appl. Phys.* **50**, 144003 (2017).
- Böhnke, T. et al. Magnetic tunnel junctions with integrated thermometers for magneto thermopower measurements. *J. Phys.: Condens. Matter* **29**, 185303 (2017).
- Böhnke, T. et al. Influence of the thermal interface resistance on the thermovoltage of a magnetic tunnel junction. *Phys. Rev. B* **95**, 104441 (2017).

14. Huebner, T. et al. Comparison of laser-induced and intrinsic tunnel magneto-Seebeck effect in CoFeB/MgAl₂O₄ and CoFeB/MgO magnetic tunnel junctions. *Phys. Rev. B* **93**, 224433 (2016).
15. Huebner, T. et al. Enhancement of thermovoltage and tunnel magneto-Seebeck effect in CoFeB based magnetic tunnel junctions by variation of the MgAl₂O₄ and MgO barrier thickness. *Phys. Rev. B* **96**, 214435 (2017).
16. Huebner, T. et al. Thermal conductivity of thin insulating films determined by tunnel magneto-Seebeck effect measurements and finite-element modeling. *J. Phys. D: Appl. Phys.* **51**, 224006 (2018).
17. Boehnke, A. et al. Large magneto-Seebeck effect in magnetic tunnel junctions with half-metallic Heusler electrodes. *Nat. Commun.* **8**, 1626 (2017).
18. Kuschel, T. et al. Tunnel magneto-Seebeck effect. arXiv:1808.05638v1 (2018).
19. Shan, J. et al. Comparison of the magneto-Peltier and magneto-Seebeck effects in magnetic tunnel junctions. *Phys. Rev. B* **92**, 20414 (2015).
20. Reimer, O. et al. Quantitative separation of the anisotropic magneto thermopower and planar Nernst effect by the rotation of an in-plane thermal gradient. *Sci. Rep.* **7**, 40586 (2017).
21. Kikkawa, T. et al. Longitudinal spin Seebeck effect free from the proximity Nernst effect. *Phys. Rev. Lett.* **110**, 67207 (2013).
22. Bougiatioti, P. et al. Quantitative disentangling of the spin Seebeck, proximity-induced, and ferromagnetic-induced anomalous Nernst effect in normal-metal-ferromagnet bilayers. *Phys. Rev. Lett.* **119**, 227205 (2017).
23. Weiler, M. et al. Local charge and spin currents in magnetothermal landscapes. *Phys. Rev. Lett.* **108**, 106602 (2012).
24. Bieren, A., von Brandl, F., Grundler, D. & Ansermet, J.-P. Space- and time-resolved Seebeck and Nernst voltages in laser-heated permalloy/gold microstructures. *Appl. Phys. Lett.* **102**, 52408 (2013).
25. Brandl, F. & Grundler, D. Fabrication and local laser heating of freestanding Ni 80 Fe 20 bridges with Pt contacts displaying anisotropic magnetoresistance and anomalous Nernst effect. *Appl. Phys. Lett.* **104**, 172401 (2014).
26. Wu, H. et al. Separation of inverse spin Hall effect and anomalous Nernst effect in ferromagnetic metals. *J. Magn. Magn. Mater.* **441**, 149–153 (2017).
27. Lee, K.-D. et al. Thermoelectric signal enhancement by reconciling the spin Seebeck and anomalous Nernst effects in ferromagnet/non-magnet multilayers. *Sci. Rep.* **5**, 10249 (2015).
28. Kikkawa, T. et al. Separation of longitudinal spin Seebeck effect from anomalous Nernst effect. Determination of origin of transverse thermoelectric voltage in metal/insulator junctions. *Phys. Rev. B* **88**, 214403 (2013).
29. Meier, D. et al. Thermally driven spin and charge currents in thin NiFe₂O₄/Pt films. *Phys. Rev. B* **87**, 54421 (2013).
30. Meier, D. et al. Influence of heat flow directions on Nernst effects in Py/Pt bilayers. *Phys. Rev. B* **88**, 184425 (2013).
31. Schmid, M. et al. Transverse spin Seebeck effect versus anomalous and planar Nernst effects in permalloy thin films. *Phys. Rev. Lett.* **111**, 187201 (2013).
32. Hasegawa, K. et al. Material dependence of anomalous Nernst effect in perpendicularly magnetized ordered-alloy thin films. *Appl. Phys. Lett.* **106**, 252405 (2015).
33. Kelekci, O., Lee, H. N., Kim, T. W. & Noh, H. Anomalous Nernst effects of [CoSiB/Pt] multilayer films. *J. Magn.* **18**, 225–229 (2013).
34. Tu, S. et al. Anomalous Nernst effect in Ir 22 Mn 78 /Co 20 Fe 60 B 20 /MgO layers with perpendicular magnetic anisotropy. *Appl. Phys. Lett.* **111**, 222401 (2017).
35. Wells, J. et al. Combined anomalous Nernst effect and thermography studies of ultrathin CoFeB/Pt nanowires. *AIP Adv.* **7**, 55904 (2017).
36. Krzyczek, P. et al. Nanoscale thermoelectrical detection of magnetic domain wall propagation. *Phys. Rev. B* **95**, 220410(R) (2017).
37. Fang, C. et al. Scaling relation between anomalous Nernst and Hall effect in [Pt/Co]_n multilayers. *Phys. Rev. B* **93**, 54420 (2016).
38. Chuang, T. C., Su, P. L., Wu, P. H. & Huang, S. Y. Enhancement of the anomalous Nernst effect in ferromagnetic thin films. *Phys. Rev. B* **96**, 174406 (2017).
39. Chen, Y.-J. & Huang, S.-Y. Absence of the thermal hall effect in anomalous Nernst and spin Seebeck effects. *Phys. Rev. Lett.* **117**, 247201 (2016).
40. Meyer, S. et al. Observation of the spin Nernst effect. *Nat. Mater.* **16**, 977–981 (2017).
41. Sheng, P. et al. The spin Nernst effect in tungsten. *Sci. Adv.* **3**, e1701503 (2017).
42. Kim, D.-J. et al. Publisher Correction. Observation of transverse spin Nernst magnetoresistance induced by thermal spin current in ferromagnet/non-magnet bilayers. *Nat. Commun.* **9**, 138 (2018).
43. Müller, G. M., Münzenberg, M., Miao, G.-X. & Gupta, A. Activation of additional energy dissipation processes in the magnetization dynamics of epitaxial chromium dioxide films. *Phys. Rev. B* **77**, 020412(R) (2008).
44. Osborn, J. A. Demagnetizing factors of the general ellipsoid. *Phys. Rev.* **67**, 351–357 (1945).
45. Mizuguchi, M., Ohata, S., Uchida, K.-i, Saitoh, E. & Takanashi, K. Anomalous Nernst effect in an L1₀-ordered epitaxial FePt thin film. *Appl. Phys. Express* **5**, 93002 (2012).
46. Sakuraba, Y. et al. Anomalous Nernst effect in L1₀-FePt/MnGa thermopiles for new thermoelectric applications. *Appl. Phys. Express* **6**, 33003 (2013).
47. Mukherjee, S. et al. Role of boron diffusion in CoFeB/MgO magnetic tunnel junctions. *Phys. Rev. B* **91**, 85311 (2015).
48. Schreiber, D. K. et al. Effects of elemental distributions on the behavior of MgO-based magnetic tunnel junctions. *J. Appl. Phys.* **109**, 103909 (2011).
49. Wang, Z. et al. Atomic-scale structure and local chemistry of CoFeB-MgO magnetic tunnel junctions. *Nano Lett.* **16**, 1530–1536 (2016).
50. Jacob, K. T., Shekhar, C. & Waseda, Y. An update on the thermodynamics of Ta₂O₅. *J. Chem. Thermodyn.* **41**, 748–753 (2009).
51. Wu, Z. L., Reichling, M., Hu, X. Q., Balasubramanian, K. & Guenther, K. H. Absorption and thermal conductivity of oxide thin films measured by photothermal displacement and reflectance methods. *Appl. Opt.* **32**, 5660–5665 (1993).

Acknowledgements

The authors gratefully acknowledge financial support by the Deutsche Forschungsgemeinschaft (DFG) within the priority program SpinCaT (SPP 1538), as well as the support for the Article Processing Charge from the DFG (German Research Foundation, 393148499) and the Open Access Publication Fund of the University of Greifswald.

Author contributions

U.M., J.W. and M.M. designed and set up the experiments. U.M. performed the TMS/ANE measurements. U.M. and T.H. prepared the samples. H.U. performed the COMSOL simulations, analyzed and discussed the temperature data with U.M. and J.W. R.R.T., C.-L.C. and R.I.T. performed the magnetization dynamics experiments, analyzed and discussed the anisotropy data with U.M. and J.W., U.M. and J.W. analyzed the data and discussed the thermal effects with T.H., O.R. and T.K. U.M. and J.W. prepared the manuscript. All authors discussed the experiments and the manuscript. M.M. and A.T. coordinated the research.

Additional information

Supplementary information accompanies this paper at <https://doi.org/10.1038/s42005-018-0063-y>.

Competing interests: The authors declare no competing interests.

Reprints and permission information is available online at <http://npg.nature.com/reprintsandpermissions/>

Publisher's note: Springer Nature remains neutral with regard to jurisdictional claims in published maps and institutional affiliations.



Open Access This article is licensed under a Creative Commons Attribution 4.0 International License, which permits use, sharing, adaptation, distribution and reproduction in any medium or format, as long as you give appropriate credit to the original author(s) and the source, provide a link to the Creative Commons license, and indicate if changes were made. The images or other third party material in this article are included in the article's Creative Commons license, unless indicated otherwise in a credit line to the material. If material is not included in the article's Creative Commons license and your intended use is not permitted by statutory regulation or exceeds the permitted use, you will need to obtain permission directly from the copyright holder. To view a copy of this license, visit <http://creativecommons.org/licenses/by/4.0/>.

© The Author(s) 2018